

Tunable Autofocusing and Enhanced Trapping Forces with Circular Pearcey Airy Beams

Yi Liang^{1,*}, Liu Tan¹, Nana Liu¹, Kaijian Chen¹, Huanpeng Liang¹, Huahao Wu¹, Bingshen Luo¹, Fuxi Lu¹, Huihe Chen², Bingsuo Zou^{1,3} and Peilong Hong^{4,5,†}


¹Guangxi Key Lab for Relativistic Astrophysics, Center on Nanoenergy Research, School of Physical Science and Technology, Guangxi University, Nanning, Guangxi 530004, China

²Department of Rehabilitation, the First Affiliated Hospital of Guangxi Medical University, Nanning, Guangxi 530021, China

³School of Physical Science and Technology and School of Resources, Environment and Materials, Key Laboratory of new Processing Technology for Nonferrous Metals and Materials, Guangxi University, Nanning 530004, China

⁴School of Optoelectronic Science and Engineering, University of Electronic Science and Technology of China (UESTC), Chengdu 611731, China

⁵The MOE Key Laboratory of Weak-Light Nonlinear Photonics, Nankai University, Tianjin 300457, China

 (Received 26 July 2022; revised 10 November 2022; accepted 8 December 2022; published 5 January 2023)

We propose and demonstrate an autofocusing beam, named the circular Pearcey Airy beam (CPAB). It is found that the CPAB exhibits a superior autofocusing property, leading to an enhanced trapping force within the autofocusing region. By thoroughly analyzing the power flow and the trapping-force distribution, we present a quantitative understanding of the autofocusing properties and the trapping capabilities of the CPAB. We also show how to tune the autofocusing and trapping properties of the CPAB by adjusting the physical parameters, such as transverse scale factor, spatial offset, and exponential decay factor. Moreover, the CPAB exhibits multiple focusing peaks along the propagation direction, capable of trapping multiple particles longitudinally and periodically. These results indicate that the CPAB is promising for optical trapping and manipulations, which may be useful in various fields, including biological research and atomic physics.

DOI: [10.1103/PhysRevApplied.19.014016](https://doi.org/10.1103/PhysRevApplied.19.014016)

I. INTRODUCTION

Optical tweezer is an essential technique for non-invasively manipulating micronanoparticles, significantly advancing many research areas, such as biology and atomic physics [1–4]. To strongly trap particles, light should be tightly focused by controlling the complex amplitudes on the wave front [5], among which the simplest way is to focus a quasilplane Gaussian beam. The intrinsic property of Gaussian beam unavoidably imposes a limit to trapping force such as photodamage [5–10]. Interestingly, similar to the effect of other structure lights [5,9–12], by replacing Gaussian beam with recently developed autofocusing beam [13], the trapping force could be greatly enhanced, implying lower photodamage and significant application potentials in optical tweezers.

Autofocusing beams could maintain a low-intensity profile to propagate a certain distance and abruptly autofocus within a small focal volume with the intensity

increased by orders of magnitude without the help of lens or nonlinearity [13–18]. Within the autofocus region, the light beams show larger intensity gradient in both the longitudinal and the transversal directions, forming a deep potential well, giving rise to increased trapping force compared with the focused Gaussian beam [13]. For practical applications, the improved trapping capability with autofocusing beams offers lots of advantages for biological samples that may suffer photodamage and optical heating [5,7–9]. From then on, many variants of autofocusing beams have been proposed and demonstrated [17], which could improve the performance of optical trapping with enhanced autofocusing properties. The well-known autofocusing beam, named the radially symmetric circular Airy beam (CAB), was generated in 2010. Recently, another autofocusing beam was developed by Chen *et al.* [19], called the circular Pearcey beam (CPB). Comparing with the CAB, the autofocusing of the CPB occurs within a shorter focusing range with the autofocused peak intensity much higher. As a result, the CPB exhibits a much stronger trapping force compared with the CAB. Later, a lot of efforts have been devoted to further enhancing the

*liangyi@gxu.edu.cn

†plhong@uestc.edu.cn

autofocusing properties of the CPB, leading to the development of circular chirp Pearcey Gaussian vortex beams [20], partially coherent Pearcey-Gauss beams [21], split autofocusing Pearcey beams [22], etc.

In this work, we propose and demonstrate that hybridizing CAB and CPB can lead to a tunable and more tightly autofocusing effect, thereby suitable for enhancing trapping capability that is critical for optical tweezers. For clarity, we dub this hybridized beam as the circular Pearcey Airy beam (CPAB). The experimental and theoretical results show that this kind of autofocusing beam can be easily controlled by adjusting its transverse scale factor, spatial offset, and exponential decay factor. Moreover, the CPAB inherits the oscillating autofocus of the CAB, which does not exist for the CPB. The significantly enhanced trapping force (twice larger than that with the CPB), together with the oscillating autofocus character, make the CPAB a promising candidate for trapping and manipulating individual particles, as well as multiple particles along the propagation direction [24]. Our results present a comprehensive understanding of the optical properties and dynamics of the CPAB in both theory and experiment, opening opportunities for optical manipulation based on optical tweezers.

II. TURNABILITY AND ENHANCEMENT OF AUTOFOCUSING OF CPAB

The proposed CPAB at the source plane is expressed as

$$\psi(r, 0) = A_0 \text{Ai}\left(\frac{r_0 - r}{w}\right) \exp\left(a \frac{r_0 - r}{w}\right) \text{Pe}\left(\frac{-r}{w}, s\right) q(r). \quad (1)$$

where A_0 is the amplitude, and the second and third terms represent the finite-energy CAB, while the last two terms represent the CPB. $\text{Ai}(x) = \int_{-\infty}^{\infty} \exp(i(t^3/3 + xt)) dt$ is the Airy function, $\text{Pe}(u, v) = \int_{-\infty}^{\infty} \exp(i(t^4 + ut^2 + vt)) dt$ is the Pearcey function. $r = \sqrt{x^2 + y^2}$ is the radial coordinate, where x and y are the transversal coordinates. w and s are the transverse scale factors to adjust the initial intensity distribution, r_0 denotes the spatial offset of the Airy function, and a is an exponential decay factor.

$q(r) = \begin{cases} 1 & r \leq r_1 \\ 0 & r > r_1 \end{cases}$ is an indicator used to limit the power

and the region of the beam. It is clear that the CPAB is a combination of the CAB and the CPB, but exhibits quite different autofocusing properties and trapping forces as shown in the following.

The input field distribution of the CPAB at the source plane is totally described by Eq. (1), which leads to unique autofocusing properties of the CPAB. To give a detailed analysis on the autofocusing properties, we calculate the

propagation of the CPAB under different conditions by employing the split-step Fourier method [25–28]. To compare the autofocusing and trapping forces with the CPB (potentially shows stronger trapping forces than the CAB [19]), the incident light powers are kept the same (here 1 W) for all cases in the calculations for clarity.

A. Tuning the exponential decay factor and the spatial offset

In our theoretical analysis and experiments hereafter, the light wavelength is kept as $\lambda = 532$ nm. First, we let $w = 100$ μm , $s = 0$, $r_1 = 1.1$ mm, but change the exponential decay factor a at different spatial offset r_0 . The peak intensity at focal point I_{max} and focal length f_z of the CPAB are shown in Figs. 1(a) and 1(b). As a increases, the focal peak intensity I_{max} decreases and focal length f_z becomes longer. Interestingly, as r_0 increases, the focal peak intensity I_{max} undergoes a growing oscillation variation until $r_0 = 350$ μm where the focal peak intensity I_{max} reaches a maximum. As r_0 grows larger than 350 μm , I_{max} rapidly falls off. The shadow area (marked by black scattering dots) in Fig. 1(a) indicates the appropriate parameters' range to modulate the CPAB to realize a stronger focal peak intensity than the corresponding CPB (same w). Meanwhile, theoretical analysis shows that the f_z of the CPAB is always shorter than the CPB.

Based on above analysis, we take $r_0 = 350$ μm , $a = 0.01$ to generate a CPAB experimentally. Our experimental setup is similar to the off-axis hologram method like Ref. [26], as depicted in Fig. 1(c). An expanded quasiplane Gaussian beam is launched to pass through a spatial light modulator (SLM, Holoeye-LC 2012), and the designed complex amplitude of the CPAB is loaded on the wave front of the light beam via the hologram method, implemented with a 4- f system. The autofocusing propagation of the generated CPAB is measured by a charge-coupled device (CCD, Daheng Optics). The experimental results are shown in Figs. 1(d1)–1(d3). At the source plane, the profile of the CPAB consists of a series of rings and the innermost two rings have the largest intensity [Fig. 1(d1)]. When propagating to the distance $z = 156$ mm, the CPAB automatically focuses with a focal peak intensity maximum [Figs. 1(d2) and 1(d3)]. For simplicity, the intensity images of the experimental results are normalized with the maximum value. By comparing with the peak intensity at the autofocusing point, the peak intensity at the input ($z = 0$ mm) is smaller than 0.01. After the focal point, the CPAB experiences an oscillating propagation while its peak intensity quickly falls off compared with the autofocusing peak intensity [Fig. 1(d3)]. These results demonstrate the strong autofocusing effect and the longitudinal oscillating autofocusing peaks of the proposed CPAB. Besides, the experimental results agree with our theoretical predictions as shown in the insets in Figs. 1(d1),

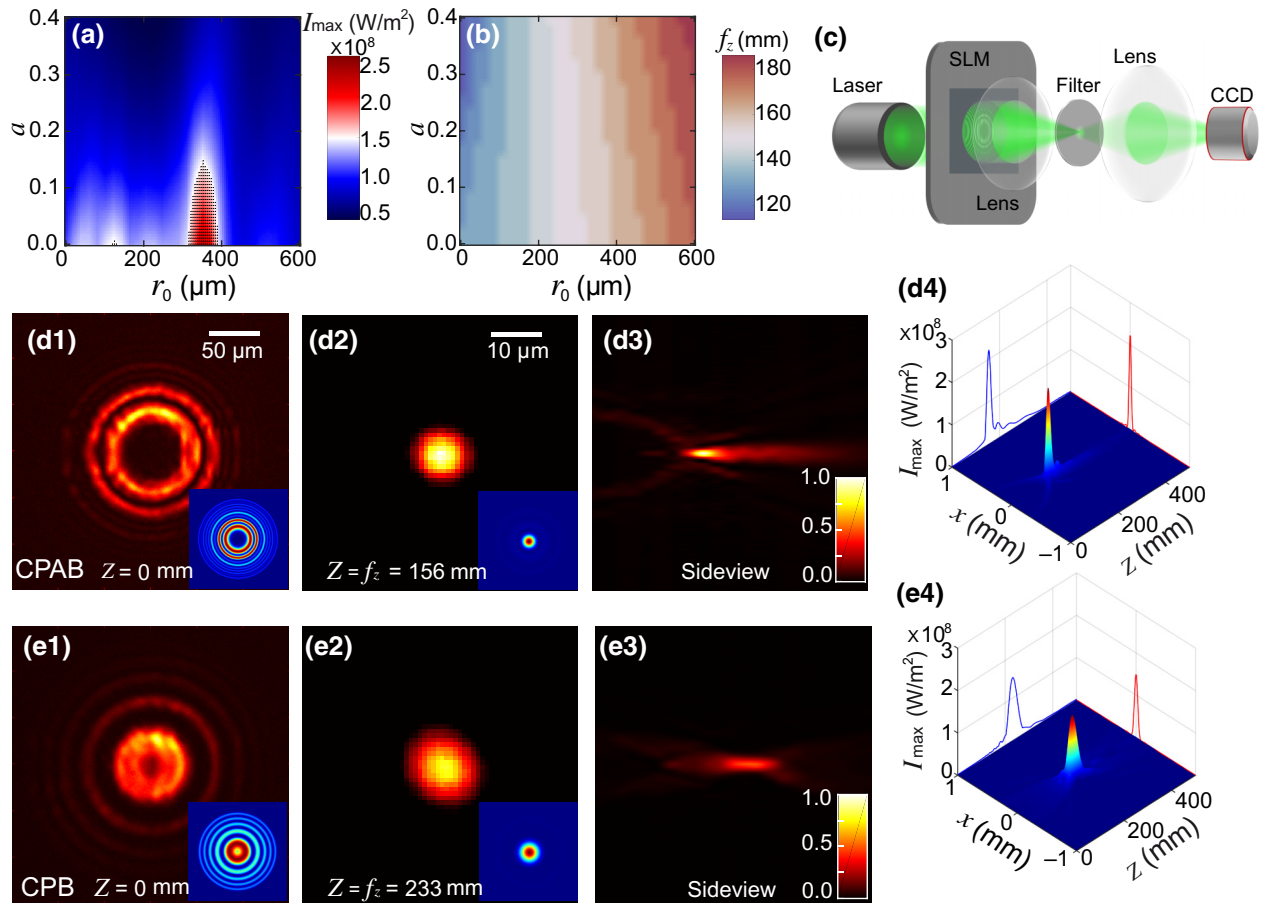


FIG. 1. Focal peak intensity I_{\max} and (b) autofocusing length f_z of the CPABs with different a and r_0 . Shadow area marked by black scattering dots indicate the appropriate parameters range to realize a stronger focal peak intensity than the CPB; (c) Schematic diagram of the experiment setup. Experimental results (hot colormap) and theoretical results (jet colormap) about propagations and intensity profiles of the CPAB (d1)–(d4) and the CPB (e1)–(e4). (d1)–(e1) Results at the source plane $z = 0$ mm, (d2)–(e2) Autofocusing results at $z = f_z$. (d3–e3) and (d4)–(e4) Sideview propagation, showing the different autofocusing properties of the two beams. Here, blue curves indicate the longitudinal intensity profiles; Red curves describe the lateral intensity distributions at focal point. The intensities in (d1),(e1) are enlarged about 100 times for better visualization while (e2) are enlarged twice. Amplitude and phase of the CPAB are shown in the Sec. 1 of Supplemental Material [23].

1(d2) and 1(d4). Through theoretical analysis, the intensity contrast of the autofocusing peak ($2.2 \times 10^8 \text{ W/m}^2$) to the maximum intensity at the source plane ($1.3 \times 10^6 \text{ W/m}^2$) is found more than 100.

For comparison, the propagation and autofocusing properties of the CPB with a same w is also presented here [Figs. 1(e1)–1(e4)]. The CPB has half the number of rings in comparison to the CPAB, and the width of the corresponding ring is twice as large at the input plane [Figs. 1(d1) and 1(e1)]. We note that their initial peak intensities at the input plane are almost equal. Generally, the autofocusing spots of these beams mainly come from the shrinking of the main ring of these beams, where the shrinking is ultimately determined by the particular complex wave front at the source plane. As a result, the CPAB produces a smaller spot size. and focal intensity of the CPB is 50% less than that of the CPAB [Figs. 1(d2) and 1(e2)].

Moreover, no oscillating propagation after the focal point appears in the propagation of the CPB [Figs. 1(e3) and 1(e4)], different from the CPAB. We also calculate their Poynting vector and analyze its internal transverse power flow, which further explains different propagation dynamics between the CPAB and the CPB (see Fig. S2 within the Supplemental Material [23]).

B. Tuning the transverse scale factor and the spatial offset

Moreover, the autofocusing of the CPAB can be further tuned by jointly changing the transverse scale factor w and the spatial offset r_0 . The results about peak intensity at focal point I_{\max} and focal length f_z are shown in Figs. 2(a1) and 2(a2) (here we take the case of $a = 0.01$ as an example for the analysis). The results show that, as

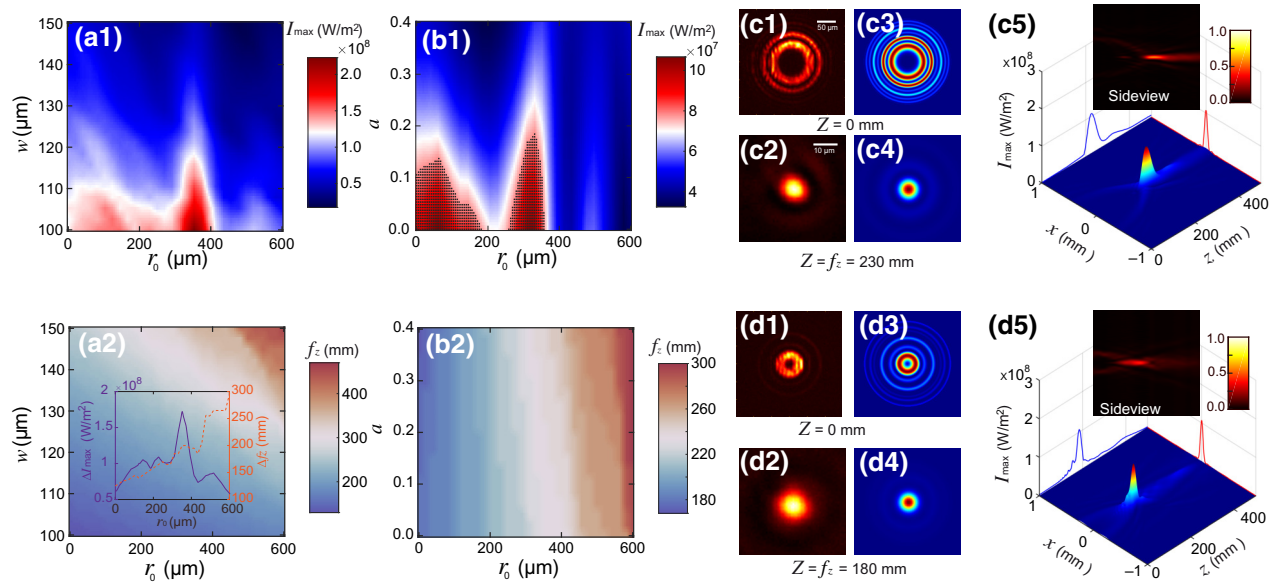


FIG. 2. Focal peak intensity I_{\max} (a1)–(b1) and autofocusing length f_z (a2)–(b2) of the CPAB with different w , a , and r_0 . Shadow area marked by black scattering dots indicate the appropriate parameters' range to realize a stronger focal peak intensity than the CPB. Inset in (a2) indicates the largest changes of focal peak intensity (cyanine curve) and autofocusing length (light brown curve) against w at different r_0 ; (c1)–(c4) and (d1)–(d4) describe the experimental (hot colormap) and the theoretical (jet colormap) results about propagations and intensity profiles of the CPAB with different r_0 [$r_0 = 350 \mu\text{m}$ for (c1)–(c4), and $r_0 = 62 \mu\text{m}$ for (d1)–(d4)]. (c1)–(d1) and (c3)–(d3) show the results at $z = 0 \text{ mm}$. (c2)–(d2) and (c4)–(d4) show the results at $z = f_z$. (c5), (d5) show the sideview propagation of the beams, where the blue curves indicate the longitudinal intensity profiles, and the red curves describe the lateral intensity distributions. For better visualization, the intensities in (c1), (c3), (d1), (d3) are enlarged about 100 times while (c2), (d2) are enlarged twice.

the transverse scale factor w increase, the focal peak intensity becomes weaker and focal length becomes longer. Particularly, these changes against the transverse scale factor w are different at different r_0 , as shown in the inset of Fig. 2(a2). The largest drop in focal peak intensity happens at $r_0 = 350 \mu\text{m}$. In this case, the largest focal peak intensity is not exactly at $r_0 = 350 \mu\text{m}$ as in Sec. II A. For example, when $w = 120 \mu\text{m}$ and $a = 0.01$, focal peak intensity I_{\max} reaches a maximum, i.e., $1.0635 \times 10^8 \text{ W/m}^2$ at $r_0 = 62 \mu\text{m}$ [Fig. 2(b1)] although focal peak intensity ($1.0633 \times 10^8 \text{ W/m}^2$) at $r_0 = 350 \mu\text{m}$ is very close to this value.

To further demonstrate the above autofocusing properties, we experimentally generate two CPABs with $r_0 = 350 \mu\text{m}$ [Fig. 2(c)] and $r_0 = 62 \mu\text{m}$ [Fig. 2(d)], respectively. Meanwhile, the theoretical results are shown for comparison. At $r_0 = 350 \mu\text{m}$, the CPAB exhibits less but wider rings as w increases compared with Figs. 1(d1)–1(d4) with the same r_0 , leading to a wider focal point as shown in Figs. 2(c1)–2(c4). The main power of the CPABs stays at the inner two rings at the source plane. The CPAB with $r_0 = 62 \mu\text{m}$ shows a shorter focal length, and the power at the input plane mostly locates at the innermost ring. Both of the demonstrated CPABs have very close focal peak intensities and focal point sizes, as predicted

by the theory. Besides, Fig. 2(b) shows that the autofocusing properties of the CPAB can be tuned by exploring other parameters, and the autofocusing peak intensity can be much stronger than the CPB (same w) with proper beam parameters.

Based on the above theoretical analysis and experimental results, it is seen that the autofocusing properties of CPABs can be flexibly tuned by adjusting the exponential decay factor a , the transversal scale factor w , and spatial offset r_0 , and we summarize here: (i) a is used to control the decay of intensity from the main ring to side rings. A larger a makes all rings get less power and the peak autofocusing intensity decreases because the focal point of autofocusing beams comes from these inward rings. (ii) w tunes the diameter and width of rings. A larger w leads to an increased diameter with the number of rings reduced in a fixed distribution area, and also widens the width of rings. Thus, a larger w produces a lower focal peak intensity, a longer autofocusing propagation and a larger focal point. (iii) r_0 controls the diameter of rings, and a larger r_0 gives rise to a longer focal length. Furthermore, r_0 decides which ring dominates the main power of the CPAB. As r_0 increase, the second inner ring starts to increase its intensity, narrowing the dark gap from the first inner ring. After passing a critical r_0 , the peak intensity of the second inner

ring may still be weaker than that of the first ring, but it has a larger diameter with more total power. Consequently, the second ring starts to contribute the main power for autofocusing. This power shift related to r_0 is responsible for the complicated oscillating autofocusing peak intensity of the CPAB.

III. SUPERIOR TRAPPING PERFORMANCE OF CPAB

The unique autofocusing properties make the CPAB interesting for optical trapping and manipulation in optical tweezers. The trapping forces acting on Rayleigh particles includes the gradient force and the scattering force, and they are formulated as [1,23]

$$F_g = \frac{1}{4}\varepsilon_0\varepsilon_m\text{Re}(\alpha)\nabla|\psi^2|, F_s = \frac{1}{6\pi c}\varepsilon_m^3k_0^4|\alpha^2|S, \quad (2)$$

where ε_0 is the permittivity in vacuum, c is the light speed in vacuum, $\alpha = 4\pi R^3(\varepsilon_p - \varepsilon_m)/(\varepsilon_p + 2\varepsilon_m)$ is the polarizability, R is the radius of the particle, $k_0 = 2\pi/\lambda$ is the

wave vector, S is the Poynting vector, ε_p and ε_m are the dielectric permittivity of particle and medium, respectively. Next, we theoretically calculate the trapping forces with the CPAB for a polystyrene bead ($R = 50$ nm) in the water ($\varepsilon_p = 2.5$, $\varepsilon_m = 1.7$) and compare the results with those for the CPB.

Figures 3(a) and 3(b) present the transversal gradient force and scattering force at the focal point for the CPAB and the CPB, and the beam parameters are the same as those used in Fig. 1. We see that the CPAB exhibits twice stronger gradient force and six times stronger scattering force than the CPB does. This trapping force enhancement is even stronger than that of the focal peak intensity enhancement. This is due to different autofocusing properties of the two kinds of beams: Firstly, from Eq. (2), the gradient force is determined by intensity gradient. As shown in Fig. 1, the CPAB has a larger focal peak intensity and a smaller focal point size than the CPB. Therefore, the CPAB shows a much larger intensity gradient, leading to the twice enhanced gradient force. Due to the CPB having higher intensity and gradient than the CAB (close to

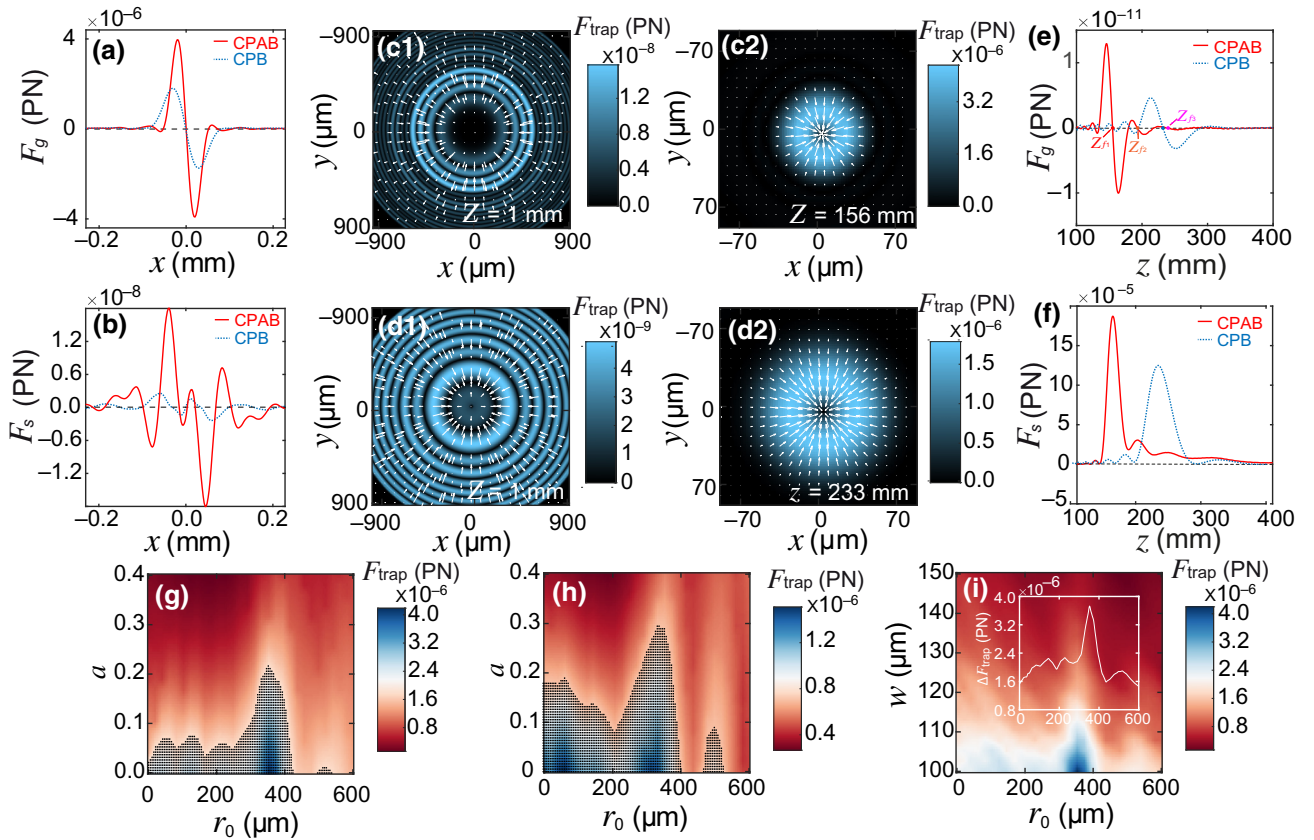


FIG. 3. The transversal gradient force (a) and the transversal scattering force (b) of the CPAB (red line) and the CPB (blue line) at the focal point. The calculated spatial distribution of the transversal trapping force of the CPAB (c1),(c2) and the CPB (d1),(d2) at initial and focal positions. The longitudinal gradient force (e) and scattering force (f) of the CPAB and the CPB. (g)–(i) Trapping forces of the CPAB with different beam parameters: (g) $w = 100$ μm , a and r_0 change; (h) $w = 120$ μm , a and r_0 change; (i) $a = 0.01$, w and r_0 change. The shadow areas by black scattering dots indicate the corresponding parameters' ranges where the CPAB have a larger trapping force than the CPB does. Inset in (i) indicates the largest changes of trapping force against w at different r_0 .

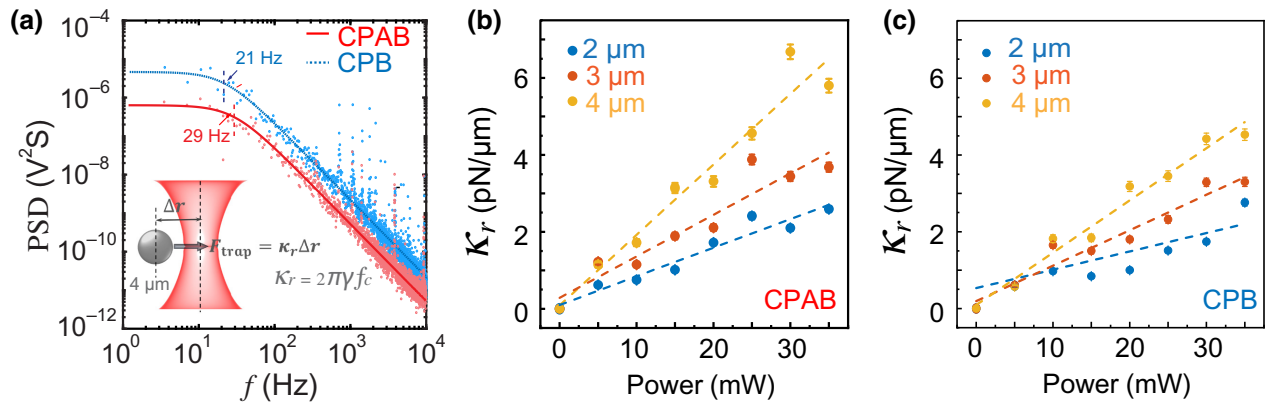


FIG. 4. (a) Power spectra of the CPAB and the CPB when they trap a single 4- μm polystyrene bead in water at 30-mW power. Inset shows the schematic diagram of particle trapping. (b),(c) Measured trap stiffnesses of the CPAB and the CPB when trapping different sizes of beads as a function of power.

the Airy-beam array) [19,29]. One can infer that the CPAB also shows a much stronger trapping force than the CAB (see Sec. S4 within the Supplemental Material [23]). Secondly, from Eq. (2), the scattering force depends on power flow. By analyzing the power flow of both beams (see Sec. S2 within the Supplemental Material [23]), the focal peak power flow of the CPAB is found exactly six times larger than that of CPB, explaining the six times stronger scattering force. Notably, gradient force is much stronger than scattering force.

To further analyze the trapping properties, we also calculated the total trapping force distributions at initial and focal positions ($\vec{F}_{\text{trap}} = \vec{F}_g + \vec{F}_s$), as shown in Figs. 3(c) and 3(d). The CPAB has twice the number of rings and less than half the ring width than the CPB does at the source plane [Figs. 3(c1) and 3(d1)]. The largest peak trapping force of the CPAB locates at the second and third inner ring while that of the CPB still keeps a nearly uniform distribution. In addition, the directions of the trapping forces at the adjacent rings are always opposite and the trapping positions appear in the dark ring between these two rings. At the focal point, the peak trapping force has 2 orders of magnitude enhancement and mainly concentrate in the center as shown in Figs. 3(c2) and 3(d2). All the directions point to the center, such that the center is the only stable trapping position. Particularly, the total trapping force is mainly contributed by gradient force, and therefore the trapping force of the CPAB is 2 times larger than the CPB.

Next, we investigate how the gradient force at the focal point changes with a and r_0 . Not surprisingly, the changes are qualitatively similar to the trend of intensity: while $w = 100 \mu\text{m}$, the trapping force decreases with an increasing a and the force is largest at $r_0 = 350 \mu\text{m}$ [Fig. 3(g)]. Before $r_0 = 350 \mu\text{m}$ the force experiences a growing oscillation variation and rapidly drops down after $r_0 = 350 \mu\text{m}$. However, the shadow area, where the force is larger than

the CPB, is quantitatively bigger than that of the focal intensity shown in Fig. 1. The same results are observed for Fig. 3(h) with $w = 120 \mu\text{m}$. In Fig. 3(h), the trapping force shows a damping descent first before $r_0 = 200 \mu\text{m}$, then rapidly goes up to a maximum at $r_0 = 350 \mu\text{m}$, and finally decays rapidly. In this case, the largest force is not located at $r_0 = 350 \mu\text{m}$, and the same result is demonstrated in Fig. 3(i).

Furthermore, we compare the longitudinal trapping forces of the CPAB and the CPB, as presented in Figs. 3(e) and 3(f). The CPAB exhibits twice stronger gradient force and 1.5 times stronger scattering force than the CPB. Meanwhile, due to the oscillating propagation, the CPAB offers multiple longitudinal trapping positions (marked by circle dots), different from the CPB. The 1st trapping position of the CPAB is at the focal point ($z_{f1} = 156 \text{ mm}$). The 2nd and 3rd positions are at $z_{f2} = 193 \text{ mm}$, $z_{f3} = 237 \text{ mm}$, respectively. A more detailed analysis on the trapping forces for the 2nd and 3rd focal points can be found in Sec. S3 within the Supplemental Material [23].

Finally, to experimentally demonstrate the above enhanced trapping capability of the CPAB, we utilize the CPAB and the CPB as optical tweezers to trap polystyrene beads with different sizes in water. Similar to Refs. [6,7], the experiment for trapping beads is schematically shown in Fig. S5 within the Supplemental Material [23]. The CPAB (or CPB) is generated at the focal plane of lens 4 (source plane of the CPAB and CPB), and then is relayed to the sample by using a 4- f imaging system composed of lens 5 and oil lens. Here, after we introduce a beam into a normal microscopic system via the 4- f imaging system composed by lens 5 and oil lens, we let the autofocusing positions appear right at the focal point of oil lens by changing the distances between lens 4 and lens 5. Thus, optical tweezers based on CPABs and CPBs are realized for trapping polystyrene beads. Then, we use power-spectrum methods to analyze the trap stiffnesses of

the beams (more detail can be found in Sec. S5 within the Supplemental Material [23]).

Our results are shown in Fig. 4. When the input power of beam is 30 mW and the size of trapping bead is 4 μm , the corner frequency f_c (~ 29 Hz) of the CPAB is larger than that of the CPB (approximately 21 Hz) [Fig. 4(a)]. Following $\kappa_r = 2\pi\gamma f_c$, the CPAB (approximately 7 pN/ μm) has larger trap stiffness than the CPB (approximately 5 pN/ μm). Accordingly, the CPAB shows a stronger trapping force ($F_{\text{trap}} = \kappa_r \Delta r$), as predicted in theory. However, the experimental result does not reach the same twice improvement as in theoretical analysis for Rayleigh particles (size is much smaller than wavelength) [Fig. 3], since the size of the experimental polystyrene bead is larger than wavelength. In this case, the full-wave generalized Lorenz-Mie theory and Maxwell stress-tensor technique [7,30] are used to calculate the trapping force and stiffness. Then, the theoretical results are consistent with our experimental results (see more detail in Sec. S6 within the Supplemental Materials [23]). Furthermore, when we change the input power and the size of trapping beads, the CPAB keeps larger trap stiffnesses than the CPB while trap stiffnesses are almost proportional to the power and increase with a bigger trapping beads [Figs. 4(b), and 4(c)]. Besides, since the $4-f$ imaging configuration composed by a tube lens and an oil objective lens demagnifies only the complex wave front at the focal plane, the demagnified beam after the objective lens still preserves the propagation properties of the autofocusing beam in free space, including exhibiting multiple forces, as demonstrated in the Video S1 within the Supplemental Material [23]. In this case, CPAB can offer multiple longitudinal trapping positions in experiment.

IV. CONCLUSIONS

In conclusion, we demonstrate that the proposed CPAB exhibits unique autofocusing features and stronger trapping force both theoretically and experimentally. By studying the propagation dynamics and power flow of the CPAB, we show that the autofocusing and trapping forces of the CPAB are tunable by controlling transverse scale factor, spatial offset, and exponential decay factor. By analyzing the tunable autofocusing dynamics, it is shown that trapping forces of the CPAB can be much larger than that of the CPB. Moreover, the longitudinal oscillating autofoci of the CPAB inherited from the CAB offers the possibility to trap multiple particles longitudinally. Our results bring the possibility of developing optical manipulation tools based on autofocusing beams for biomedical applications, such as accessing the deformability of cells, sensing microstructure, and reducing the photodamage on biological samples [1,8,10].

ACKNOWLEDGMENTS

The author thanks the support from National Natural Science Foundation of China (11604058), Guangxi Natural Science Foundation (2020GXNSFAA297041, 2020GXNSFDA238004), Innovation Project of Guangxi Graduate Education (YCSW2022041), the Natural Science Foundation of Sichuan Province (23NSFSC0415), the Fundamental Research Funds for the Central Universities (ZYGX2020J010), and the Open Project Funding of the Ministry of Education Key Laboratory of Weak-Light Nonlinear Photonics (OS22-1).

-
- [1] P. Jones, O. Maragò, and G. Volpe, *Optical Tweezers: Principles and Applications* (Cambridge University Press, Cambridge, 2015).
 - [2] G. Pesce, P. H. Jones, O. M. Maragò, and G. Volpe, Optical tweezers: Theory and practice, *Eur. Phys. J. Plus* **135**, 949 (2020).
 - [3] J. Gieseler, J. R. Gomez-Solano, A. Magazzù, I. Pérez Castillo, L. Pérez García, M. Gironella-Torrent, X. Viader-Godoy, F. Ritort, G. Pesce, A. V. Arzola, K. Volke-Sepúlveda, and G. Volpe, Optical tweezers - from calibration to applications: A tutorial, *Adv. Opt. Photon.* **13**, 74 (2021).
 - [4] D. G. Grier, A revolution in optical manipulation, *Nature* **424**, 810 (2003).
 - [5] Y. Yuanjie, R. Yuxuan, C. Mingzhou, A. Yoshihiko, and R.-G. Carmelo, Optical trapping with structured light: A review, *Adv. Photon.* **3**, 034001 (2021).
 - [6] F. Lu, L. Tan, Z. Tan, H. Wu, and Y. Liang, Dynamical power flow and trapping-force properties of two-dimensional Airy-beam superpositions, *Phys. Rev. A* **104**, 023526 (2021).
 - [7] F. Lu, H. Wu, Y. Liang, L. Tan, Z. Tan, X. Feng, Y. Hu, Y. Xiang, X. Hu, Z. Chen, and J. Xu, Bessel-modulated autofocusing beams for optimal trapping implementation, *Phys. Rev. A* **104**, 043524 (2021).
 - [8] Y. Liang, G. Liang, Y. Xiang, J. Lamstein, R. Gautam, A. Bezryadina, and Z. Chen, Manipulation and Assessment of Human Red Blood Cells with Tunable Tug-of-War Optical Tweezers, *Phys. Rev. Appl.* **12**, 064060 (2019).
 - [9] H. Rubinsztein-Dunlop, *et al.*, Roadmap on structured light, *J. Opt.* **19**, 013001 (2017).
 - [10] A. I. Bunea and J. Glückstad, Strategies for Optical Trapping in Biological Samples: Aiming at Microrobotic Surgeons, *Laser Photon. Rev.* **13**, 1800227 (2019).
 - [11] R. A. B. Suarez, A. A. R. Neves, and M. R. R. Gesualdi, Optical trapping with non-diffracting Airy beams array using a holographic optical tweezers, *Opt. Laser Technol.* **135**, 106678 (2021).
 - [12] R. A. B. Suarez, L. A. Ambrosio, A. A. R. Neves, M. Zamboni-Rached, and M. R. R. Gesualdi, Experimental optical trapping with frozen waves, *Opt. Lett.* **45**, 2514 (2020).
 - [13] Y. F. Jiang, K. K. Huang, and X. H. Lu, Radiation force of abruptly autofocusing Airy beams on a Rayleigh particle, *Opt. Express* **21**, 24413 (2013).

- [14] N. K. Efremidis and D. N. Christodoulides, Abruptly autofocusing waves, *Opt. Lett.* **35**, 4045 (2010).
- [15] D. G. Papazoglou, N. K. Efremidis, D. N. Christodoulides, and S. Tzortzakis, Observation of abruptly autofocusing waves, *Opt. Lett.* **36**, 1842 (2011).
- [16] P. Zhang, J. Prakash, Z. Zhang, M. S. Mills, N. K. Efremidis, D. N. Christodoulides, and Z. Chen, Trapping and guiding microparticles with morphing autofocusing Airy beams, *Opt. Lett.* **36**, 2883 (2011).
- [17] N. K. Efremidis, Z. Chen, M. Segev, and D. N. Christodoulides, Airy beams and accelerating waves: An overview of recent advances, *Optica* **6**, 686 (2019).
- [18] D. Li, D. Bongiovanni, M. Goutsoulas, S. Xia, Z. Zhang, Y. Hu, D. Song, R. Morandotti, N. K. Efremidis, and Z. Chen, Direct comparison of anti-diffracting optical pin beams and abruptly autofocusing beams, *OSA Continuum* **3**, 1525-1535 (2020).
- [19] X. Y. Chen, D. M. Deng, J. L. Zhuang, X. Peng, D. D. Li, L. P. Zhang, F. Zhao, X. B. Yang, H. Z. Liu, and G. H. Wang, Focusing properties of circle Pearcey beams, *Opt. Lett.* **43**, 3626 (2018).
- [20] X. Chen, D. Deng, G. Wang, X. Yang, and H. Liu, Abruptly autofocused and rotated circular chirp Pearcey Gaussian vortex beams, *Opt. Lett.* **44**, 955 (2019).
- [21] X. Zhou, Z. Pang, and D. Zhao, Partially coherent Pearcey-Gauss beams, *Opt. Lett.* **45**, 5496 (2020).
- [22] F. Wang and Y. Liang, Split autofocusing Pearcey beams with flexible trapping capabilities, *Opt. Commun.* **484**, 126681 (2021).
- [23] See Supplemental Material at <http://link.aps.org/supplemental/10.1103/PhysRevApplied.19.014016> for details of amplitude, phase, power flow, trapping force at the second and third longitudinal trapping positions of the CPABs, comparison with circular Airy beams, trapping bead experiments, theoretical trapping performance with non-Rayleigh particles, animation and videos of the beams' propagation and trapping.
- [24] Z. Zhang, P. Zhang, M. Mills, Z. Chen, D. N. Christodoulides, and J. L. Liu, Trapping aerosols with optical bottle arrays generated through a superposition of multiple Airy beams, *Chin. Opt. Lett.* **11**, 033502 (2013).
- [25] Y. Liang, Y. Hu, Z. Ye, D. Song, C. Lou, X. Zhang, J. Xu, R. Morandotti, and Z. Chen, Dynamical deformed Airy beams with arbitrary angles between two wings, *J. Opt. Soc. Am. A* **31**, 1468 (2014).
- [26] Y. Chen, X. Lin, S. Lin, S. Mo, L. Wan, and Y. Liang, Propagation dynamics of deformed 2D vortex Airy beams, *Chin. Opt. Lett.* **15**, 080801 (2017).
- [27] Y. Liang, Y. Chen, and L. Wan, Propagation and power flow of high-order three-Airy beams, *Opt. Commun.* **405**, 120 (2017).
- [28] Y. Liang, Y. Hu, D. Song, C. Lou, X. Zhang, Z. Chen, and J. Xu, Image signal transmission with Airy beams, *Opt. Lett.* **40**, 5686 (2015).
- [29] R. A. B. Suarez, A. A. R. Neves, and M. R. R. Gesualdi, Optimizing optical trap stiffness for Rayleigh particles with an Airy array beam, *J. Opt. Soc. Am. B* **37**, 264 (2020).
- [30] H. Wu, X. Zhang, P. Zhang, P. Jia, Z. Wang, Y. Hu, Z. Chen, and J. Xu, Optical pulling force arising from non-paraxial accelerating beams, *Phys. Rev. A* **103**, 053511 (2021).